A&A, 702, A172 (2025)
https://doi.org/10.1051/0004-6361/202554808

Astronomy & Astrophysics

Primordial black holes in the main lensing galaxy of FBQ 0951+2635

Daniel Isla[1,⋆], Luis J. Goicoechea[1,2,⋆], Ana Esteban-Gutiérrez[3], Vyacheslav N. Shalyapin[1,2,4], Rodrigo Gil-Merino[5], Jose M. Diego[2], and Eleana Ruiz-Hinojosa[1]

[1] Departamento de Física Moderna, Universidad de Cantabria, Avda. de Los Castros s/n, E-39005 Santander, Spain
[2] Instituto de Física de Cantabria (CSIC-UC), Avda. de Los Castros s/n, E-39005 Santander, Spain
[3] Instituto de Física y Astronomía, Universidad de Valparaíso, Avda. Gran Bretaña 1111, Valparaíso, Chile
[4] O.Ya. Usikov Institute for Radiophysics and Electronics, National Academy of Sciences of Ukraine, 12 Acad. Proscury St., UA-61085 Kharkiv, Ukraine
[5] Escuela Superior de Ingeniería y Tecnología, Universidad Internacional de La Rioja (UNIR), Avda. Gran Vía Rey Juan Carlos I 41, E-26005 Logroño, Spain

Received 27 March 2025 / Accepted 26 August 2025

ABSTRACT

Although dark matter in galaxies may consist of elementary particles different from those that make up ordinary matter and that would be smoothly distributed (still undetected), the so-called primordial black holes (PBHs) formed soon after the initial Big Bang are also candidates to account for a certain fraction of mass in galaxies. In this paper, we focus on the main lensing galaxy ($z = 0.260$) of the doubly imaged, gravitationally lensed quasar FBQ 0951+2635 ($z = 1.246$) for probing possible PBH populations. Assuming that the mass of the galaxy is due to smoothly distributed matter (SDM), stars, and PBHs, the 16-yr microlensing variability observations were compared in detail with simulated microlensing signals generated by 90 different physical scenarios. Among other details, the simulated signals were sampled as the observed one, and the observed variability in its entirety and over the long term were used separately for comparison. While none of the scenarios considered can reproduce the overall observed signal, the observed long-term variability favours a small mass fraction in PBHs with a mass of the order of the mean stellar mass. Furthermore, it is possible to obtain strong constraints on the galaxy mass fraction in Jupiter-mass PBHs, provided that a reverberation-based measurement of the source size is available and relatively small. To constrain the mass fraction in $\sim 10\,M_\odot$ PBHs, light curves five times longer are probably required.

Key words. gravitational lensing: micro – galaxies: halos – dark matter – quasars: individual: FBQ 0951+2635

1. Introduction

In the last quarter of the 20th century, several pioneering studies presented compelling evidence for the presence of significant amounts of dark matter in galaxy halos (e.g. Rubin et al. 1978, 1980). Despite all efforts to identify the composition of this invisible dark matter, its nature is still unknown. While tens of elementary particles have been proposed as possible dark-matter candidates (e.g. Bertone 2010), primordial black holes (PBHs) formed in the early Universe are non-luminous astrophysical objects that could also populate galaxy halos and be part of the dark matter on galaxy scales (e.g. Carr & Kühnel 2022).

For the Milky Way and the Large Magellanic Cloud, strong constraints on the fraction of dark matter in planetary-mass and stellar-mass PBHs were derived through microlensing variability of stars in the Milky Way's biggest satellite galaxy. A recent analysis revealed that possible PBHs in the mass range of 1.8×10^{-4}–$6.3\,M_\odot$ would make up $\leq$1% of dark matter in these two galaxies, and that hypothetical populations of PBHs in the mass window 10–$100\,M_\odot$ cannot account for more than 3% of dark matter (Mróz et al. 2024). Therefore, gravitational microlensing observations indicate that planetary-mass and stellar-mass PBHs may only account for a small fraction of dark matter in both local galaxies.

Primordial black holes in non-local galaxies can also be detected from gravitational-wave experiments (if they belong to coalescing binary systems) or from their gravitational microlensing effects on background compact sources. For example, the discovery of gravitational waves from non-local black-hole binaries by the LIGO-Virgo collaboration (e.g. Abbott et al. 2019) suggested the possibility that some of these black holes were formed in the early Universe. For the ten confidence detections of black-hole binaries of Abbott et al. (2019), the typical mass of black holes varied between 8 and $50\,M_\odot$, and they were located in the $0.1 \leq z \leq 0.5$ redshift interval. However, the microlensing variability of a distant star ($z = 1.49$) in the field of the galaxy cluster MACSJ1149.5+2223 ($z = 0.54$) favoured a small mass fraction of the intracluster medium in $\sim 30\,M_\odot$ PBHs (e.g. Kelly et al. 2018; Diego et al. 2018). Additionally, differential microlensing magnifications between pairs of images of lensed quasars indicated that the lensing galaxy mass in PBHs in the LIGO-Virgo mass window must be $\leq$1% at the 90% confidence level (Esteban-Gutiérrez et al. 2022).

Microlensing in gravitationally lensed quasars is sensitive to possible populations of PBHs in lensing galaxies and has a great potential to constrain these populations (e.g. Vernardos et al. 2024, and the previous paragraph). In this vein,

⋆ Corresponding authors: disla003@ikasle.ehu.eus, goicol@unican.es

microlensing-induced energy shifts of the Fe Kα emission line in three lensed quasars indicated that planetary-mass PBHs cannot compose more than 0.01−0.03% of the total mass of the lensing galaxies at $z \sim 0.3$ and 0.7 (Dai & Guerras 2018; Bhatiani et al. 2019). However, single-epoch fluxes of samples of lensed quasars suggested that PBHs with substellar masses of 0.082 and 0.0024 $M_\odot$ could constitute up to ∼15% and ∼60% of the total mass at the 90% confidence level, respectively (Esteban-Gutiérrez et al. 2023). In addition, stars and star-like PBHs (with masses close to the mean stellar mass) can only amount to about 10−20% of the total mass (e.g. Mediavilla et al. 2009, 2017).

Although observed microlensing variability of lensed quasars may also provide critical clues about the dark-matter composition in lensing galaxy halos, recent studies have led to inconclusive or contradictory results. Using microlensing variations in six lensed quasars monitored for ∼10 years by the COSMOGRAIL collaboration, Awad et al. (2023) found that a standard scenario with only stellar microlenses (absence of PBHs) cannot be rejected. They also could not reject a scenario in which all dark matter in the galaxies at $0.3 \leq z < 0.9$ is due to stellar-mass PBHs. However, Hawkins (2020) reached a very different conclusion, claiming that stellar-mass PBHs are required to explain amplitudes of microlensing signals in lensed quasars. Additionally, we highlight that these dark objects would be distributed either inside the lensing galaxies or along the lines of sight to the quasars, the latter possibility being supported by light curves and emission lines of non-lensed quasars (Hawkins 2022, 2024).

However, it is not a straightforward task to accurately simulate microlensing effects of a cosmologically distributed population of PBHs at different redshifts between a distant quasar and the observer. Also, the putative PBHs are expected to be concentrated at mass-density peaks harbouring massive galaxies. Thus, we focused on a standard framework based on the presence of PBHs in main lensing galaxies of gravitationally lensed quasars. In this paper, we discuss the feasibility of different populations of PBHs in the main lensing galaxy of the doubly imaged quasar, FBQ 0951+2635 (Schechter et al. 1998), from a detailed analysis of its microlensing variability. In Sect. 2, we present lensing mass solutions and observed microlensing curves spanning 16 years (2008−2023). Sect. 3 describes our methodology, which basically relies on the comparison between observed and synthetic (simulated) microlensing signals. Results are included in Sect. 4, and our conclusions are summarised in Sect. 5.

2. FBQ 0951+2635: Lensing mass solutions and observed difference light curves

We selected FBQ 0951+2635 (Schechter et al. 1998) as a case study to learn about the potential of microlensing variability to constrain populations of PBHs in lensing galaxies. The brightest optical image of the double quasar is denoted by the letter A, while the faintest optical image and the main lensing galaxy are denoted by B and G, respectively. In a pioneering work on this lens system, Jakobsson et al. (2005) reported a quasar redshift of 1.246, a solution for the astrometry of ABG and the ellipticity of G (based on near-IR observations with the *Hubble* Space Telescope)[1], a flux ratio of $B/A = 0.21 \pm 0.03$ at 8.4 GHz, and a time delay between both quasar images of 16 ± 2 d (A is leading). The 16-d delay relied on optical light curves from October 2000 to June 2001. Additionally, the redshift of G ($z = 0.260$) was spectroscopically measured by Eigenbrod et al. (2007).

2.1. Lensing mass solutions

Using all the observational constraints of the system in the previous paragraph along with a flat ΛCDM cosmology with $H_0 = 70\,\mathrm{km\,s^{-1}\,Mpc^{-1}}$, $\Omega_M = 0.3$, and $\Omega_\Lambda = 0.7$, it is possible to model the lensing mass as a singular power-law ellipsoid (SPLE) describing the gravitational effects of G plus external shear (ES) due to intervening galaxies other than G. In this approach, the external convergence (EC or κ_{ext}) is assumed to be negligible. The corresponding lensing mass solution (Ruiz-Hinojosa 2023) allowed us to estimate the total convergence (κ), the total shear strength (γ), and the shear direction (θ_γ) at the positions of A and B (see the second row in Table 1). Unfortunately, regarding the astro-photometric solution of Jakobsson et al. (2005), there is evidence that the effective radius of the light distribution of G is severely underestimated (Sluse et al. 2012; Shalyapin et al. 2025). In addition to this 'size problem' of the elliptical light halo, Rivera et al. (2023) suggested the existence of a disc, which was not considered in most previous solutions. Hence, due to the current ambiguity in the galaxy light distribution, we cannot use tight constraints on the convergence in stars.

To check the influence of the time delay and mass model on our final results, we also considered a second approach (see the third row in Table 1). Since the 16-d delay from a short monitoring campaign has been questioned (e.g. Eulaers & Magain 2011; Rathna Kumar et al. 2015), we used light curves from the Nordic Optical Telescope (1999−2001; Jakobsson et al. 2005; Paraficz et al. 2006), the Kaj Strand Telescope (2008−2017; Rivera et al. 2023), and the Liverpool Telescope (2009−2023; initial light curves were presented by Gil-Merino et al. 2018) to measure a more robust delay of 13.3 ± 1.7 d. This time-delay interval practically coincides with that of Shalyapin et al. (2025). In addition, Wilson et al. (2017) conducted a spectroscopic survey of galaxies along the line of sight towards FBQ 0951+2635, showing evidence of an EC above 0.17. Taking into account the new constraint on the time delay, the lower limit of $\kappa_{ext} = 0.17$, and the model Hubble constant of $H_0/(1-\kappa_{ext})$, Ruiz-Hinojosa's mass solution (SPLE+ES model) is still usable as an 'effective' solution. It is also easy to show that the total convergence is $\kappa = \kappa_G + \kappa_{ext}$, where $\kappa_G = (1-\kappa_{ext}) \times \kappa_{eff}$ is the actual convergence produced by G and κ_{eff} is the overestimated value of the SPLE+ES effective solution. Similarly, the total shear strength is $\gamma = (1-\kappa_{ext}) \times \gamma_{eff}$, with γ_{eff} being the effective shear strength (for definitions of the convergence and shear and their effective or scaled versions, see e.g. Schneider et al. 1992; Grogin & Narayan 1996).

2.2. Observed microlensing signals

Microlensing signals are derived from difference light curves, and the main idea is as follows. The flux of the quasar image B at time t is given by $F_B(t) = F_I(t)\epsilon_B\mu_B(t)$, where F_I is the intrinsic quasar flux, ϵ_B is the dust extinction factor, and μ_B is the lens magnification. This lens magnification may vary over time as a result of microlensing effects. Similarly, after taking into account the time delay between the two quasar images (Δt), the flux of A verifies $F_A(t-\Delta t) = F_I(t)\epsilon_A\mu_A(t)$. To remove the intrinsic signal and convert fluxes to magnitudes, we compute the flux

[1] These observations (Kochanek et al. 2000) yielded other astro-photometric solutions (e.g. Sluse et al. 2012; Rivera et al. 2023), and here we do not consider different constraint sets through the same observations. However, the controversy on the galaxy light distribution is discussed in Sect. 2.1.

Table 1. Convergence and shear parameters for FBQ 0951+2635.

Approach	κ_A	γ_A	θ_{γ_A}	κ_B	γ_B	θ_{γ_B}
First	0.279	0.380	36.3	1.194	1.352	49.9
Second	0.401	0.315	36.3	1.161	1.122	49.9

Notes. In the first approach, we considered a 16-d time delay and a SPLE+ES mass model, whereas the second approach relies on a shorter delay of 13.3 d and a SPLE+ES+EC mass model (see the main text). The shear direction (θ_γ) is given in degrees east of north.

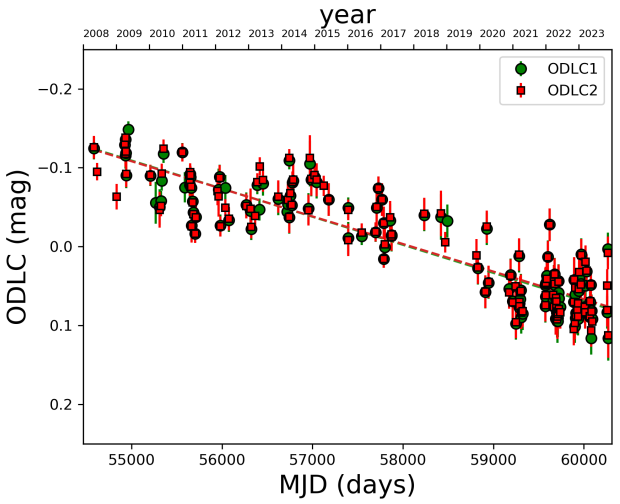

Fig. 1. Observed difference light curves of FBQ 0951+2635 in the r band. They are built from time-delay values of 16 d (ODLC1) and 13.3 d (ODLC2). For each delay, the light curve of A is time shifted, and its shifted magnitudes around the dates in B were interpolated and subtracted from the magnitudes of B. The final step is to subtract the average magnitude difference. We also show two linear fits (green and red dashed lines) to the observed microlensing signals (although they can barely be distinguished from each other in the plot).

ratio, take its logarithm, and multiply by −2.5. The resulting magnitude difference can be written as

$$B(t) - A(t-\Delta t) = -2.5 \log\left[\frac{F_B(t)}{F_A(t-\Delta t)}\right] = -2.5 \log\left[\frac{\epsilon_B \mu_B(t)}{\epsilon_A \mu_A(t)}\right]. \quad (1)$$

By subtracting the 16-yr average magnitude difference from Eq. (1), it is also possible to remove dust extinction effects. Therefore, we obtain

$$B(t) - A(t-\Delta t) - \langle B(t) - A(t-\Delta t)\rangle = -2.5 \left\{\log\left[\frac{\mu_B(t)}{\mu_A(t)}\right] - \left\langle \log\left[\frac{\mu_B(t)}{\mu_A(t)}\right]\right\rangle\right\}. \quad (2)$$

Given the observed light curves $A(t)$ and $B(t)$, as well as a time-delay measurement of Δt, the expression on the left side of Eq. (2) allows us to build an observed difference light curve (ODLC). In the absence of microlensing effects, $\mu_B(t)/\mu_A(t)$ would remain constant and equal to the macro-magnification ratio, which means that the ODLC should be zero at all times.

We built two ODLCs using the two delay values corresponding to the approaches given in Table 1. Regarding the quasar light curves, we used GLENDAMA+ brightness records of FBQ 0951+2635 until 1 December 2023 (Shalyapin et al. 2025), which were complemented with magnitudes at the two additional epochs MJD = 58925.941 and 60266.264. These records mainly consist of r-band magnitudes provided by observations with the Liverpool Telescope (GLENDAMA project; Gil-Merino et al. 2018) and the Kaj Strand Telescope (Rivera et al. 2023), and they cover a period of 16 years from 2008−2023. Despite the availability of earlier monitorings in the R band (e.g. Jakobsson et al. 2005; Paraficz et al. 2006; Shalyapin et al. 2009), we focused on well-sampled r-band light curves without significant gaps (see data availability). The two ODLCs are displayed in Figure 1. There is a very high degree of similarity between both observed microlensing signals (green circles and red squares in Figure 1) since the correlation coefficient is 0.996.

The ODLCs of FBQ 0951+2635 show a long-term variability (see the two linear fits in Figure 1) along with rapid fluctuations around it. This short-timescale (rapid) variability could be due to standard microlensing of a compact source, observational noise, or physics that is ignored during the modelling discussed in Sect. 3. There is growing evidence that both the compact accretion disc and the broad line region of some lensed quasars contribute significantly to their optical band fluxes (e.g. Gil-Merino et al. 2018; Paic et al. 2022; Fian et al. 2023), such that the rapid variability in the corresponding ODLCs may be correlated with intrinsic short-term variations (see Fig. 4 of Goicoechea et al. 2024).

3. Methodology

3.1. Magnification maps

We compared the ODLCs and synthetic difference light curves (SDLCs) from source trajectories on simulated magnification maps. These magnification maps for each quasar image were made using a Fortran-90 code based on the Poisson and inverse polygon (PIP) method (see data availability), and a simpler version addressing a single population of microlenses is described in Shalyapin et al. (2021). The analysis was carried out according to two approaches (already detailed in Sect. 2). Our first approach assumes that the convergence is exclusively due to the lensing galaxy G ($\kappa_{ext} \sim 0$), so it can be decomposed into three contributions (e.g. Esteban-Gutiérrez et al. 2022): smoothly distributed matter (SDM) in the galaxy halo (κ_{sdmG}), stars (κ_{starG}), and PBHs (κ_{pbhG}). Thus, in addition to the convergence and shear strength, the SDM mass fraction $f_{sdmG} = \kappa_{sdmG}/\kappa_G$ and the ratio $F_{pbhG} = \kappa_{pbhG}/(\kappa_{starG} + \kappa_{pbhG})$ are two other parameters of the PIP software. Once f_{sdmG} and F_{pbhG} have been fixed, finding the mass fractions of the two microlens populations, i.e., $f_{pbhG} = F_{pbhG}(1 - f_{sdmG})$ and $f_{starG} = 1 - F_{pbhG}(1 - f_{sdmG}) - f_{sdmG}$, is straightforward. In this case study, we considered a grid consisting of three relevant values of f_{sdmG}: 0.1 (microlens dominated mass), 0.5, and 0.9 (SDM dominated mass), and four values of F_{pbhG}: 0 (standard scenarios), 0.1, 0.5, and 0.9.

For the second approach, the convergence due to SDM includes both the contribution from G (κ_{sdmG}) and that from galaxy-group halos acting as secondary deflectors (κ_{ext}). These groups are located near G and along the line of sight to the quasar (Wilson et al. 2017). More specifically, $f_{sdm} = \kappa_{ext}/\kappa + f_{sdmG}(1 - \kappa_{ext}/\kappa)$, where f_{sdmG} is the SDM mass of G relative to its total mass (see above). We again took the 2D grid $\{[f_{sdmG}], [F_{pbhG}]\} = \{[0.1, 0.5, 0.9], [0, 0.1, 0.5, 0.9]\}$ to be consistent with the grid used in the first approach.

With respect to the mass of the microlenses, stars are randomly distributed following a power-law mass function of

$dN/dM \propto M^{-\alpha}$ over a mass range of $M_1 < M < M_2$, where M_2/M_1 denotes the maximum-to-minimum mass ratio. Some quasar microlensing studies relied on a Salpeter mass function ($\alpha = 2.35$) with $M_2/M_1 = 100$ (e.g. Kochanek 2004; Awad et al. 2023), while others used a Kroupa mass function ($\alpha = 1.3$) with $M_2/M_1 = 50$ (e.g. Cornachione et al. 2020; Rivera et al. 2023). However, all reasonable stellar mass functions produce similar microlensing effects (e.g. Kochanek 2004), and we took a Kroupa distribution with $M_2/M_1 = 50$. We also adopted a typical mean stellar mass of $M_{\rm star} = 0.3\,M_\odot$ (e.g. Mosquera & Kochanek 2011). Due to our lack of knowledge about the properties of the other family of microlenses (PBHs), we assumed that PBHs are randomly distributed and have the same mass ($M_{\rm pbh}$), and we considered three different values of $r_{\rm pbh} = \log(M_{\rm pbh}/M_{\rm star})$. These values are $r_{\rm pbh} = -2.5$ ($M_{\rm pbh} \sim 0.001\,M_\odot$; Jupiter-mass PBHs), -0.5 ($M_{\rm pbh} \sim 0.1\,M_\odot$), and 1.5 ($M_{\rm pbh} \sim 10\,M_\odot$; PBHs with stellar black-hole mass).

We built square magnification patterns of $40\,R_{\rm E}$ on a side, where $R_{\rm E} = 3.76 \times 10^{16}$ cm is the Einstein radius in the source plane of a $0.3\,M_\odot$ star (for a flat ΛCDM cosmology; see Sect. 2.1). These magnification maps contain 8000×8000 pixels. However, since the quasar source responsible for the observed r-band fluxes has a finite size, each magnification pattern was convolved with a Gaussian brightness profile of $I(R) \propto \exp(-R^2/2R_{\rm s}^2)$, where $R_{\rm s}$ is the source radius. In this work, we considered the two values of $R_{\rm s}$ that were derived from previous fits of r-band and H-band/r-band microlensing variations (Rivera et al. 2023), as well as a smaller value for comparison purposes (to better check the influence of the source size). Hence, by defining the relative radius as $r_{\rm s} = R_{\rm s}/R_{\rm E}$, we used $r_{\rm s} = 0.605$ (fit of r-band data), 0.276 (joint fit of H-band and r-band data), and 0.1 (about 15 Schwarzschild radii for an $8.9 \times 10^8\,M_\odot$ supermassive black hole; e.g. Peng et al. 2006). To prevent edge effects (Gaussian convolution biases), pixels near the sides of the convolved maps were not considered for subsequent analysis. The unbiased map regions contain 7200×7200 pixels ($36\,R_{\rm E}$ on a side) and allow us to make large numbers of synthetic light curves with an appropriate resolution (see Sect. 3.2).

As a summary, using the parameter values in Table 1 and those detailed in this section, for each approach and quasar image, we generated a total of 90 magnification maps, nine of which are associated with standard scenarios without PBHs (3 SDM mass fractions × 3 source sizes) and 81 of which correspond to non-standard scenarios (3 SDM mass fractions × 3 PBHs mass to microlenses mass ratios × 3 PBH masses × 3 source sizes). The combinations of parameters that produce the total of 90 physical scenarios are illustrated in Table A.1. For some scenarios, we verified that one large map per approach and image is sufficient, as another large map from a different spatial distribution of microlenses produces similar results. In Figure 2, we show map examples for both images using the first approach. The top panels include magnification patterns for a standard scenario with 10% of mass in stars ($f_{\rm sdmG} = 0.9$), and the other panels display maps for non-standard scenarios consisting of 45% of the mass in Jupiter-mass PBHs ($f_{\rm sdmG} = 0.5$; second row), 81% of the mass in PBHs with a mass similar to those of low-mass red dwarfs and high-mass brown dwarfs ($f_{\rm sdmG} = 0.1$; third row), and 45% of the mass in PBHs with $M_{\rm pbh} \sim 10\,M_\odot$ ($f_{\rm sdmG} = 0.5$; fourth row). In the four scenarios, the intermediate-size source ($r_{\rm s} = 0.276$) was considered.

3.2. Simulated difference light curves

For a given image, we note that the shear direction forms an angle θ_γ with the celestial north, so its magnification maps are constructed using a 2D coordinate system in which one of the two axes coincides with this particular (shear) direction. Therefore, the coordinate axes for A and B do not match, and sometimes the map of one of the two images is conveniently rotated to analyse source trajectories across the sky on the maps of both images (e.g. see Fig. 2 of Paic et al. 2022), whereas other times the source trajectories on one of the two maps are rotated (our procedure; see below). For each scenario (set of values of $f_{\rm sdmG}$, $F_{\rm pbhG}$, $r_{\rm pbh}$, and $r_{\rm s}$) in the two approaches, the magnification patterns for images A and B were used to draw source trajectories and obtain their associated SDLCs. In order to have an adequate sample size, we generated 10^5 synthetic difference records for each pair of AB maps (see Sect. 3.3).

We estimated the effective transverse velocity of the source ($v_{\rm e}$) from Eq. (5) of Mosquera & Kochanek (2011). This effective motion provides crucial information in the time domain, since it links the length of a path travelled by the source (in the source plane) to the time elapsed in the observer's rest frame. Additionally, it depends on the redshifts of the main deflector and source, the cosmological model, and the transverse peculiar velocities of the observer, main deflector, and source, as well as on the velocity dispersion of the microlenses in G. Using the redshifts and cosmology given in Sect. 2, and the peculiar motions and microlens velocity dispersion taken from Rivera et al. (2023), we inferred a value of $v_{\rm e} = 8.94 \times 10^7$ cm s^{-1}. It is important to mention that $v_{\rm e}$ is basically due (95% of the total) to the motion of G and microlenses within G, so its direction is unknown, and thus we can assume source trajectories with arbitrary orientations.

Regarding the construction of a SDLC for a source trajectory on a pair of AB maps, we took a random point (x_1, y_1) on the map for A and generated a random trajectory angle (orientation) α in the interval $[0, 2\pi]$. The straight path of the source on this A map can then be mathematically described as

$$\begin{aligned} x(t) &= x_1 + R(t)\cos\alpha \\ y(t) &= y_1 + R(t)\sin\alpha, \end{aligned} \tag{3}$$

where (x_1, y_1) represents the initial source position ($t = 0$) and $R(t) = 0.041 \times t$ is the path length (in pixels) travelled after a time t (in days). We calculated the time differences $t_k = {\rm MJD}_k - {\rm MJD}_1$ ($k = 1, \ldots, N$) for the N epochs in the corresponding ODLC (see Figure 1), which allowed us to construct a magnification curve, $\mu_{\rm A}(t_k)$ ($k = 1, \ldots, N$), mimicking the ODLC sampling. For a given time t_k, the source is located at (x_k, y_k), with $x_k = x(t_k)$ and $y_k = y(t_k)$. However, we note that x_k and y_k are real numbers, whereas the A map contains information in pixels (pair of natural numbers). Hence, we performed a weighted interpolation to derive the magnification at t_k: $\mu_{\rm A}(x_k, y_k) = [\sum_p \mu_{\rm A}(p) W(p)]/\sum_p W(p)$, where $\mu_{\rm A}(p)$ is the magnification in the pixel p, $W(p) = 1 - d_{pk}$ is the weight of this pixel, and d_{pk} is the distance between the pixel p and the point of interest (only pixels at distances $d_{pk} \leq 1$ are considered). In addition, equations for the straight path of the source on the B map are similar to those in Eq. (3), with an angle of $\alpha - (\theta_{\gamma_{\rm B}} - \theta_{\gamma_{\rm A}})$ and another initial position; i.e. a starting point randomly chosen on the map for B and a path that is rotated 13°.6 clockwise. After computing the corresponding magnifications $\mu_{\rm B}(t_k)$ ($k = 1, \ldots, N$) by following the procedure described above, the expression on the right side of Eq. (2) led to the SDLC.

3.3. Comparison between ODLCs and SDLCs

For a given scenario (in the first or second approach), we have to compare each SDLC with the corresponding ODLC. Here,

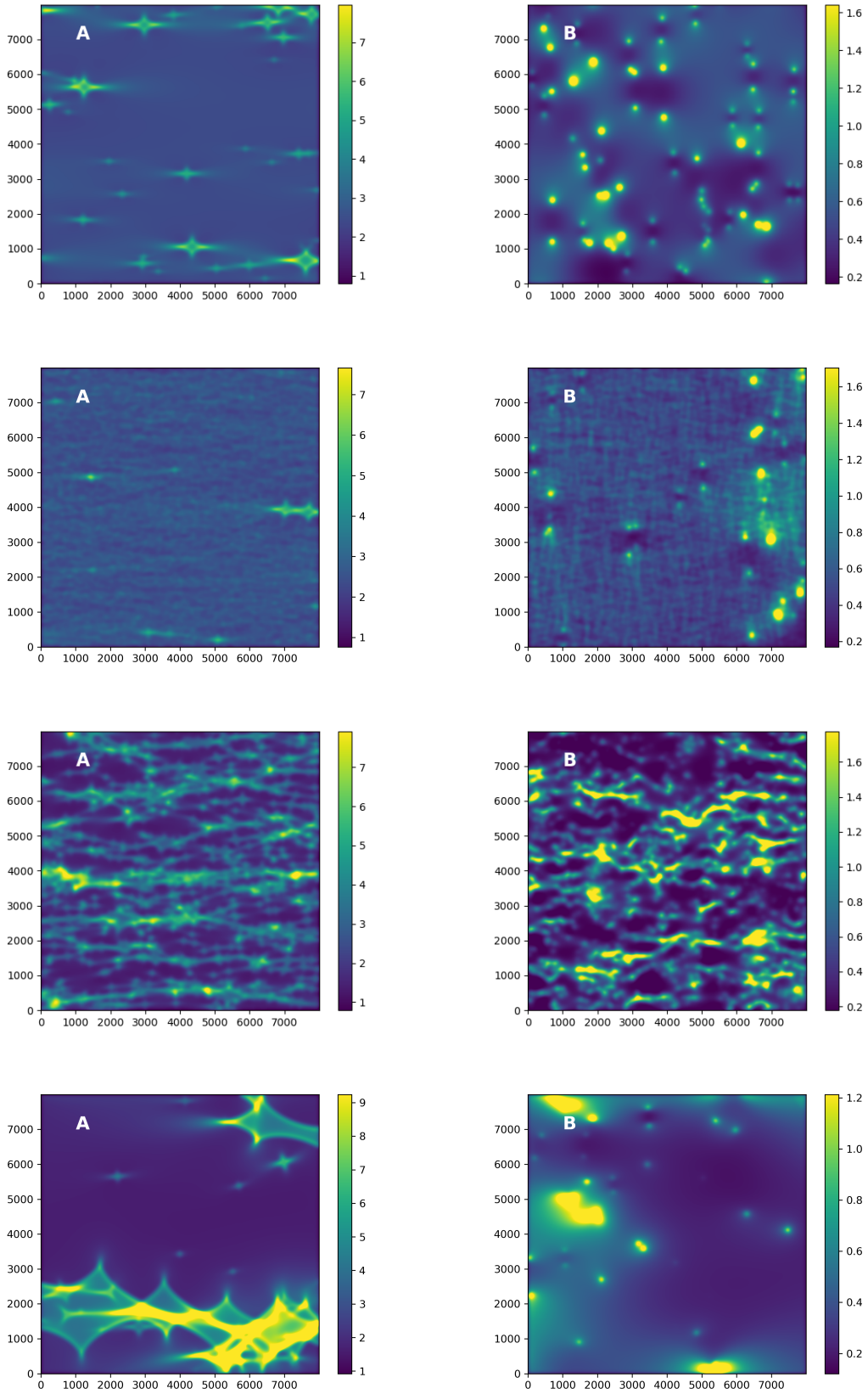

Fig. 2. Examples of magnification maps for first approach. *First row from the top*: Standard scenario without PBHs and with 90% of mass in SDM. *Second row*: Non-standard scenario with 50% of mass in SDM and 45% of mass in PBHs with $M_{\rm pbh} \sim 0.001\,{\rm M}_{\odot}$. *Third row*: Non-standard scenario with 10% of mass in SDM and 81% of mass in PBHs with $M_{\rm pbh} \sim 0.1\,{\rm M}_{\odot}$. *Fourth row*: Non-standard scenario with 50% of mass in SDM and 45% of mass in PBHs with $M_{\rm pbh} \sim 10\,{\rm M}_{\odot}$. In all scenarios, the quasar source is of intermediate size (see the main text). The colour scale represents magnification values, with 2.66 and 0.56 being the macro-magnifications of A and B, respectively.

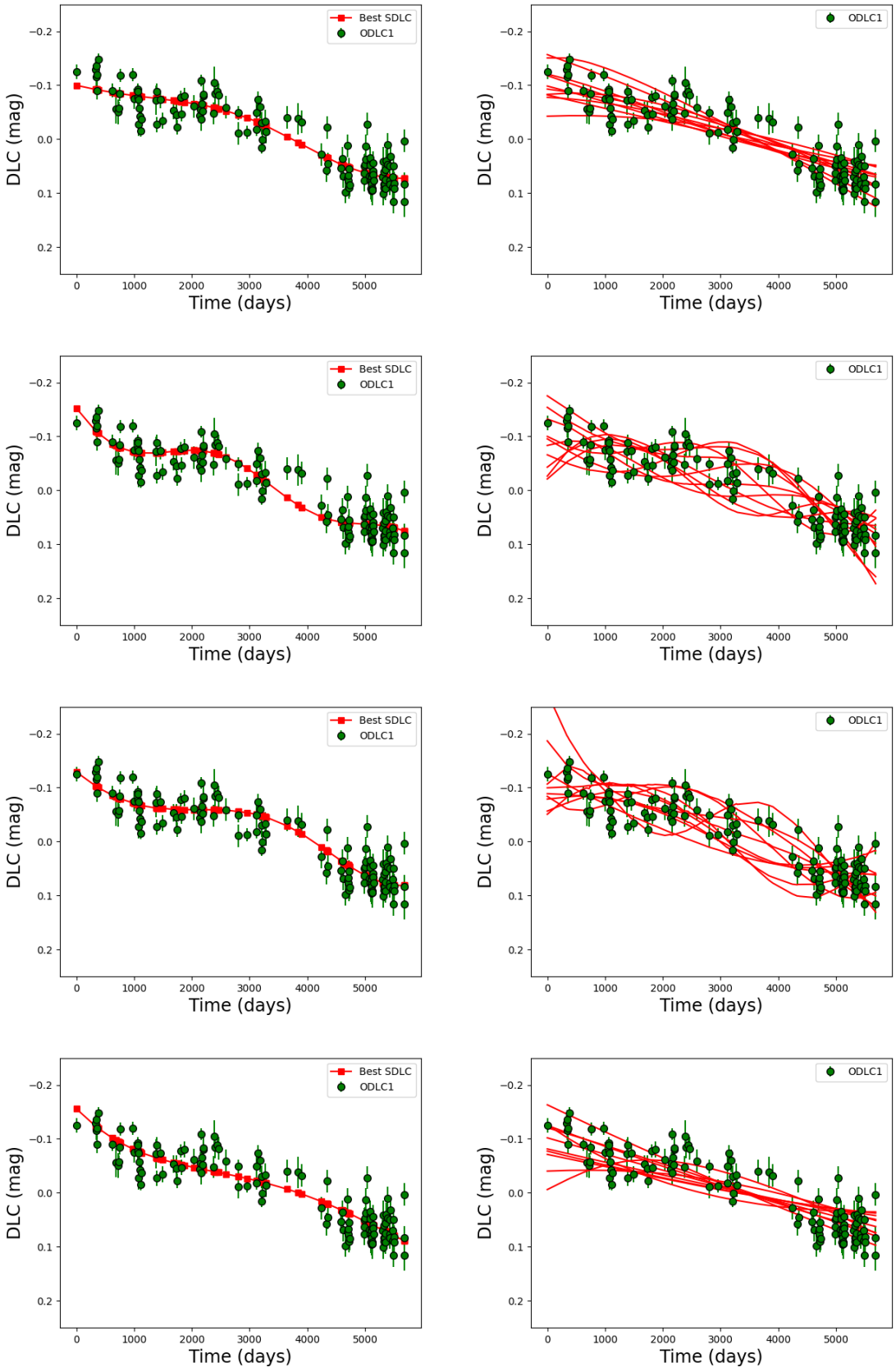

Fig. 3. Comparison between ODLC in first approach and SDLCs for all scenarios in Figure 2. After generating 10^5 SDLCs from each pair of maps, we show the best-fit SDLC (minimum RMS; left panels) and ten randomly chosen SDLCs that are characterised by RMS < 2.60 (out of a total of n; right panels). Each row corresponds to the same row position in Figure 2, so the results for the standard scenario without PBHs are depicted in the first row from the top ($RMS_{min} = 1.67$ and $n = 10\,919$), and those for the non-standard scenarios are shown in successive rows: 45% of the mass in Jupiter-mass PBHs ($RMS_{min} = 1.60$ and $n = 1536$; second row), 81% of the mass in ~0.1 $M_\odot$ PBHs ($RMS_{min} = 1.68$ and $n = 152$; third row), and 45% of the mass in ~10 $M_\odot$ PBHs ($RMS_{min} = 1.69$ and $n = 13\,381$; fourth row).

the root mean square (RMS) of relative residuals was used to assess how closely a synthetic microlensing signal matches the observed one. Since both signals consist of N data points, the RMS is given by the equation

$$\mathrm{RMS} = \sqrt{\frac{1}{N}\sum_{j=1}^{N}\left(\frac{O_j - S_j}{E_j}\right)^2}, \quad (4)$$

where O_j and E_j denote the observed differences and their errors, respectively, and S_j are the simulated values. If the RMS is ∼1, the SDLC fits the ODLC well; in other words, the SDLC is consistent with the observed data. However, the E_j values could be slightly underestimated, leading to relatively high RMS values. Thus, in a first analysis scheme, in order to account for a slight underestimation of errors and the presence of a few outliers, the ODLC-SDLC consistency threshold was set to 1.5. This means that the SDLC and corresponding ODLC are consistent with each other when RMS < 1.5. For example, if RMS = 1.5, the measured uncertainties typically represent 2/3 of real errors.

Linear fits to the ODLCs (see Figure 1) trace their slow variability quite well. However, rapid variations also appear around these fits. Due to that, in a second analysis scheme, we assumed that the rapid variability in the ODLCs of FBQ 0951+2635 is not caused by standard microlensing, and, consequently, our microlensing simulations cannot account for it. There are two plausible reasons to adopt this second scheme. First, observed rapid variations might be due to unaccounted for, unknown observational noise. Second, the observed rapid variability may be due to physics that was ignored when constructing SDLCs, and it could be correlated with the rapid intrinsic variability (see the last paragraph in Sect. 2.2 and Goicoechea et al. 2024). In both cases, simulations would only reproduce the long-timescale (slow) variability of the ODLCs, and rapid variations should be considered as additional noise.

Therefore, for each approach given in Table 1, original photometric errors were increased by a factor RMS(L), where RMS(L) is the RMS value for the linear fit to the ODLC, while we kept the consistency threshold of 1.5 to allow for a true slow signal slightly different to low-order polynomial functions that best fit the data. This is equivalent to using a ODLC-SDLC consistency threshold of 1, increasing the errors by a factor of 1.5 × RMS(L), and to using the original errors but increasing the consistency thresholds up to 1.5 × RMS(L) = 2.60 and 2.74 for the first and second approaches, respectively. To illustrate the ODLC-SDLC comparison in our second analysis scheme, Figure 3 displays the ODLC in the first approach along with well-fitted SDLCs (RMS < 2.60) from the eight example maps shown in Figure 2. The minimum RMS values barely depend on the example scenario, and they are above 1.5 and close to RMS(L) ∼ 1.7. From a statistical point of view, the second and third example scenarios have more difficulties than the other two in reproducing the underlying long-term variation, since only 10^2–10^3 out of 10^5 SDLCs fit the ODLC well.

For each scenario in both approaches, we generated N_s SDLCs, $n(\mathrm{RMS} < T)$ of which produce a RMS value less than a threshold of T. Thus, the consistency probability percentage for a threshold, T, was defined as

$$\mathrm{CP}(T) = 100 \times \frac{n(\mathrm{RMS} < T)}{N_s}, \quad (5)$$

where we considered $T = 1.5$ (first analysis scheme), and $T = 2.60$ or 2.74 (depending on the approach used; second analysis scheme). A pending issue is the choice of N_s (sample size), keeping in mind that a large number of possible source's paths is required to fully cover magnification maps and yield robust parameter estimation of RMS distributions. Some tests show that $N_s = 10^5$ provides a good compromise between robustness and computational cost, and Table 2 shows results from the two example maps in the top panels of Figure 2 (see also top panels of Figure 3). Table 2 includes uncertainties in three statistical parameters of the RMS distribution from a sample of 10^5 SDLCs: mean (⟨RMS⟩), standard deviation (σ_{RMS}), and CP(2.60). These uncertainties are standard deviations (second row) derived from ten samples of 10^5 SDLCs. It is worth noting that the uncertainty in CP(2.60) is only 0.1%. Additionally, we did not incorporate CP(1.5) into Table 2 because the consistency probability for a threshold of $T = 1.5$ is zero.

Table 2. Parameter uncertainties for a sample of size $N_s = 10^5$.

⟨RMS⟩	σ_{RMS}	CP(2.60)
±0.027	±0.045	±0.095%

Notes. Uncertainties in the mean and standard deviation of RMS values (first two columns), and in the consistency probability for a RMS threshold of 2.60 (last column; see the main text for details about the approach, scenario, and procedure to estimate uncertainties).

4. Results

Using the two approaches in Table 1, we did not find any scenario yielding SDLCs with RMS < 1.5. Therefore, CP(1.5) = 0 for the 90 physical scenarios considered in both approaches, covering a wide range of mass compositions of the galaxy, PBH masses, and source sizes. We have to emphasise here that our goal is not to achieve good fits of the observed variability in its entirety by fine tuning the microlensing parameters, but to use a limited number of microlensing parameter combinations and test how the associated scenarios perform. Although about twenty million ($2 \times 90 \times 10^5$) SDLCs failed to reproduce the overall variability of the ODLCs, several scenarios were reasonably consistent with their long-timescale variability. Figure 4 shows our results in the (⟨RMS⟩, σ_{RMS}) plane. The standard (circles) and non-standard (triangles) scenarios are classified into three categories according to their consistency with observations for the RMS thresholds described in the last paragraph of Sect. 3.3. Thus, the green circles and triangles correspond to the best scenarios with a consistency probability in the 10–20% interval. In Figure 4, as expected, these green markers are placed around or slightly above the dashed line: $\sigma_{\mathrm{RMS}} = \langle\mathrm{RMS}\rangle$. We also note that a number of non-standard scenarios (including a PBH population) are among the best.

All consistency probability values from our second analysis scheme are displayed in Figure 5. The nine panels of Figure 5 are sorted such that the SDM mass fraction increases from top to bottom, and for a given value of f_{sdmG}, the mass fraction in PBHs for non-standard scenarios increases from left to right. The open circles (first approach) and filled squares (second approach) denote probabilities for the standard scenarios with $f_{\mathrm{pbhG}} = 0$, while the dashed (first approach) and solid (second approach) lines describe probabilities for the non-standard scenarios. Examining Figure 5 in detail, one can see there is a clear analogy between the results of the two approaches, indicating that the time delay and mass model do not play a critical role in our microlensing analysis. Additionally, the consistency probability is below 3% in standard scenarios with $f_{\mathrm{sdmG}} = 0.1$, and it

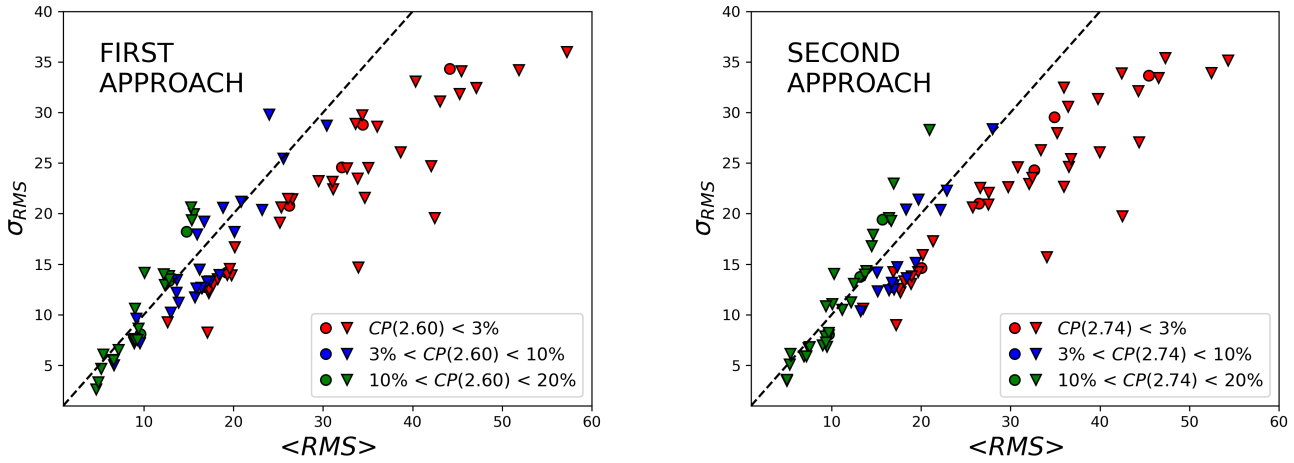

Fig. 4. Statistical properties of RMS distributions. For each approach in Table 1, we display the ⟨RMS⟩ and $\sigma_{\rm RMS}$ values associated with nine standard (circles) and 81 non-standard (triangles) physical scenarios. Three intervals of consistency probability are also highlighted in red, blue, and green (see the main text).

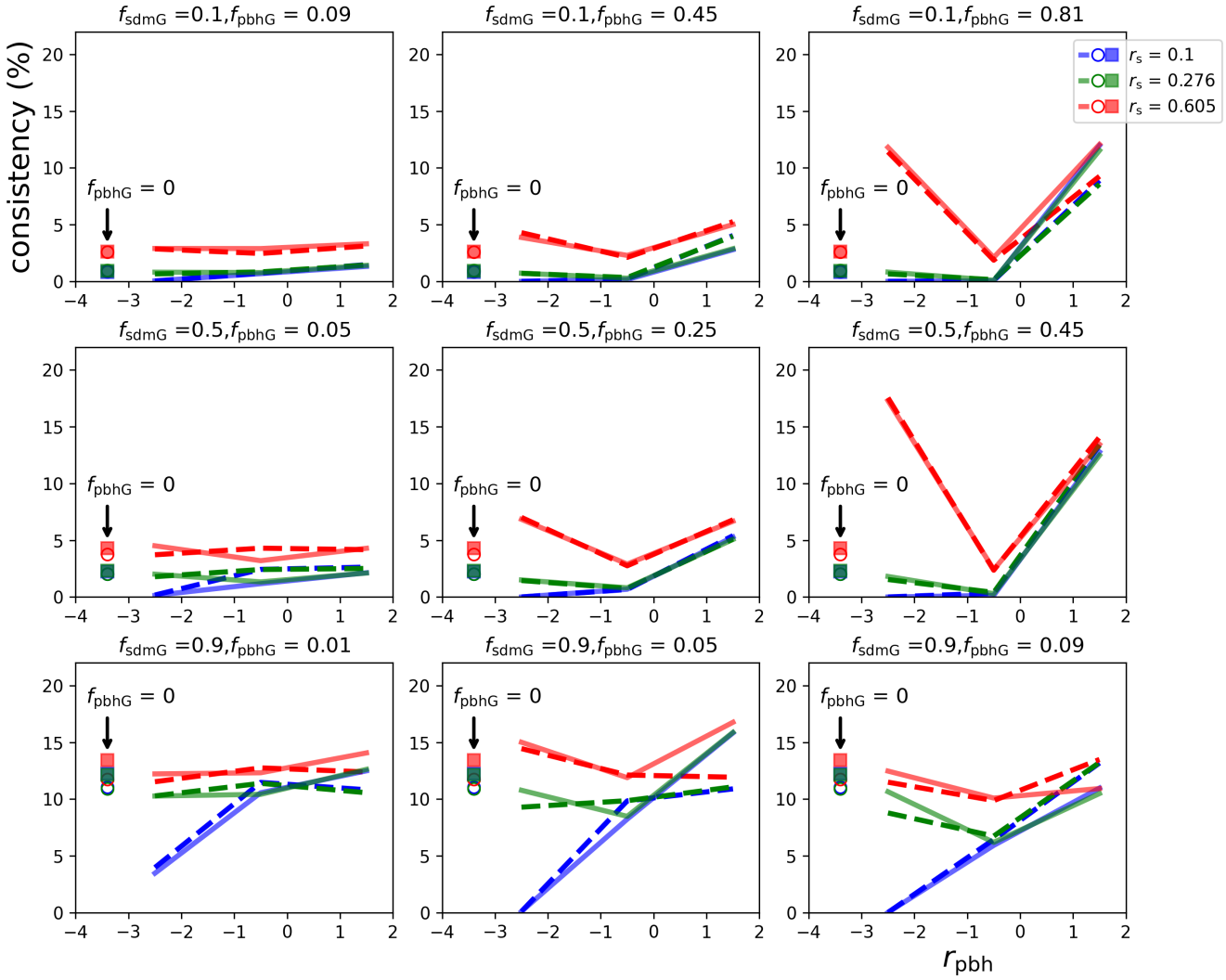

Fig. 5. Consistency probability between observed slow extrinsic variability and simulated microlensing signals in relevant physical scenarios. The open circles (standard scenarios) and dashed lines (non-standard scenarios) represent the results from the first approach, and the filled squares (standard scenarios) and solid lines (non-standard scenarios) indicate the results using the second approach. The x-axis represents the logarithm of the $M_{\rm pbh}/M_{\rm star}$ ratio and includes the three values used in the non-standard scenarios; i.e. $r_{\rm pbh} = -2.5$, -0.5, and 1.5. We arbitrarily put the results for the standard scenarios at $r_{\rm pbh} = -3.4$ for a better visual comparison. The source size is highlighted in blue, green, and red (see the main text).

only reaches values above 10% when the SDM is the dominant contribution to the mass of the galaxy. It is also worth noting that microlensing effects of PBHs with a mass close to the mean stellar mass ($r_{\rm pbh} = -0.5$ and $M_{\rm pbh} \sim 0.1\,{\rm M}_\odot$) resemble, to a large extent, those of stars; therefore, scenarios with $f_{\rm sdmG} = 0.9$ and a small mass fraction in PBHs ($f_{\rm pbhG} < 0.1$) in this PBH mass window are favoured. These results agree with the statistical analysis of microlensing magnifications for a sample of 20 lensed quasars (including FBQ 0951+2635; Mediavilla et al. 2009) and the conclusions of Esteban-Gutiérrez et al. (2023) concerning star-like PBHs.

In Figure 5, if we look at scenarios with the less massive PBHs ($r_{\rm pbh} = -2.5$ and $M_{\rm pbh} \sim 0.001\,{\rm M}_\odot$) and the largest source, it is difficult to distinguish between a population of PBHs and an equivalent amount of mass in SDM, since PBHs behave as a smooth distribution of dark matter. For example, mass compositions with $f_{\rm sdmG} = 0.1$ and $f_{\rm pbhG} = 0.45$ (top middle panel), $f_{\rm sdmG} = 0.1$ and $f_{\rm pbhG} = 0.81$ (top right panel), and $f_{\rm sdmG} = 0.5$ and $f_{\rm pbhG} = 0.45$ (middle right panel) have probabilities similar to mass compositions with $f_{\rm sdmG} = 0.5$ and $f_{\rm pbhG} = 0.05$ (middle left panel), $f_{\rm sdmG} = 0.9$ and $f_{\rm pbhG} = 0.01$ (bottom left panel), and $f_{\rm sdmG} = 0.9$ and $f_{\rm pbhG} = 0.05$ (bottom middle panel), respectively. For mass compositions of G verifying $f_{\rm sdmG} + f_{\rm pbhG} > 0.9$, the probabilities vary from 11.4% to 17.5%, while they are only about 3% for $f_{\rm sdmG} + f_{\rm pbhG} < 0.2$. In terms of consistency, it is not surprising that the best scenario out of the 90 studied is the one with the largest source and a mass fraction in Jupiter-mass PBHs of 0.45 (see the middle right panel). This means that the 'effective' SDM mass fraction is 0.95 ($f_{\rm starG} = 0.05$), in good agreement with Fig. 7 of Mediavilla et al. (2009). If we focus on the smallest source, populations of Jupiter-mass PBHs have very low probabilities, mostly below 0.1%. Hence, the constraints on the less massive PBHs strongly depend on the source size.

In addition, based on measurements of microlensing magnifications for several lensed quasars, previous studies indicated that $f_{\rm pbhG} \leq 0.01$ at the 90% confidence level for PBHs with $10\,{\rm M}_\odot$ and source sizes similar to those used in this work (e.g. Esteban-Gutiérrez et al. 2022). However, the observed slow extrinsic variability of FBQ 0951+2635 is reasonably consistent with scenarios involving small, moderate, and large mass fractions in massive PBHs ($r_{\rm pbh} = 1.5$ and $M_{\rm pbh} \sim 10\,{\rm M}_\odot$), regardless of the source size (see the bottom and right panels of Figure 5).

For completeness, using our second analysis scheme, in Appendix B we also present results of a likelihood-based Bayesian metric for both approaches. To calculate the probabilities of the 90 scenarios, their individual SDLCs were weighed by $\exp(-\chi^2/2)$ (e.g. Kochanek et al. 2007). Additionally, taking the standard scenario with $f_{\rm sdmG} = 0.9$ and the intermediate size source as a reference, the relative Bayesian probabilities (η) were compared with the relative consistency probabilities (ϵ) in Figure B.1. Although results show reasonable agreement between the two metrics, three spikes in η are observed for both approaches (highlighted with black triangles in Figure B.1) that have no counterparts in ϵ. These high-probability spikes correspond to non-standard scenarios with $f_{\rm sdmG} = 0.9$, $f_{\rm pbhG} = 0.01$–0.09, Jupiter-mass PBHs, and the intermediate size source. The three non-standard scenarios with $f_{\rm sdmG} = 0.9$, $f_{\rm pbhG} = 0.09$, and massive PBHs also lead to relatively small values of η for the second approach (see the black rectangle in the bottom panel of Figure B.1). For a given scenario, while the Bayesian metric favours the best fits to data (minimum χ^2 values), we promote the CP metric (ϵ value) because it weighs all SDLCs with a RMS below the consistency threshold equally and thus constrains the underlying signal less severely.

5. Conclusions

Since PBHs could provide a certain fraction of the mass in galaxies, several recent studies focused on the use of gravitational microlensing to probe possible PBH populations in local and non-local galaxies. Thus, planetary-mass and stellar-mass PBHs may only account for a small percentage of dark matter in the Milky Way and the Large Magellanic Cloud (e.g. Mróz et al. 2024), while the analysis of single-epoch microlensing effects of non-local (mostly early-type) galaxies acting as main gravitational lenses of distant quasars led to relevant results on Jupiter-mass, star-like, and 10–60 $\rm M_\odot$ PBHs (e.g. Mediavilla et al. 2009; Esteban-Gutiérrez et al. 2022, 2023). Microlensing effects on the Fe Kα emission region of a few lensed quasars were also used to put strong constraints on the population of substellar PBHs (mass fraction $\lesssim$0.01–0.03%; Dai & Guerras 2018; Bhatiani et al. 2019).

Although difference light curves of lensed quasars is a relatively unexplored tool to constrain PBH populations in lensing galaxies, these time-domain microlensing signals could help reveal the composition of non-local galaxies. Very recently, Awad et al. (2023) used difference light curves of several lensed quasars to shed light on the mass composition of their main lensing galaxies. However, they only discussed two different physical scenarios: a standard scenario including SDM and stars, and an alternative scenario in which all the mass is in the form of compact objects with a stellar mass function (only stars and stellar-mass PBHs, without SDM), concluding that both are consistent with the observed microlensing signals. Optical light curves of Q2237+0305 are also consistent with ~10% of the bulge mass of its main (spiral) lens galaxy being formed by planetary-mass PBHs (Tuntsov et al. 2024). In this work, as a case study, we considered difference light curves of the well-studied doubly imaged quasar FBQ 0951+2635 spanning 16 years. The observed microlensing signals have been compared to synthetic difference light curves corresponding to source trajectories on simulated magnification maps, and we thoroughly examined 90 physical scenarios covering a range of relevant mass compositions of the main lensing galaxy, PBH masses, and source sizes. The standard scenarios only include SDM and stars, whereas the non-standard ones incorporate SDM, stars, and PBHs.

The rapid variability in the observed microlensing signals cannot be explained by any of the 90 scenarios considered. Even using a sample of 10^8 SDLCs for some scenarios, we did not find RMS values below 1.5. We did, however, find several scenarios that are reasonably consistent with the observed slow microlensing variability, that is, the best standard and non-standard scenarios with consistency probabilities (as defined in the last paragraph of Sect. 3.3 and shown in Figure 5) above 10%. It is also demonstrated that the time delay and mass model adopted, provided they are reasonable, have little impact on the results. Regarding the standard scenarios, the best ones correspond to a galaxy mass dominated by SDM. Moreover, considering a PBH population with a mass close to the mean stellar mass, the best scenarios also include a dominant contribution of SDM to the galaxy mass and a relatively small mass fraction in PBHs (<10%). These results using the variability of only one lensed quasar are in good agreement with some previous single-epoch studies from tens of lens systems (e.g. Mediavilla et al. 2009, 2017).

Additionally, for the largest source, the best non-standard scenarios with Jupiter-mass PBHs correspond to a galaxy mass dominated by the contribution of the two non-stellar ingredients (SDM + PBHs), since these PBHs behave as SDM. However, for the smallest source, most scenarios with Jupiter-mass PBHs are highly unlikely, so the estimation of the source size through an independent experiment (e.g. using the continuum-reverberation mapping method; Gil-Merino et al. 2012; Mudd et al. 2018) could lead to strong constraints on the population of planetary-mass PBHs in the lensing galaxy. At the other end of the PBH-mass spectrum, some scenarios with massive PBHs ($\sim 10\,M_\odot$) have a consistency above 10%. For these best scenarios, the mass fraction in PBHs can even be ~80%. This result does not contradict the strong constraints on $10\,M_\odot$ PBHs in a previous analysis of single-epoch fluxes of a sample of lensed quasars (e.g. Esteban-Gutiérrez et al. 2022), but rather encourages the study of light curves with longer temporal coverage to try to confirm or improve current constraints according to microlensing variability. Our ODLCs describe microlensing variations on a spatial scale similar to the Einstein radius in the source plane of a $0.3\,M_\odot$ star, which is equivalent to about 20% of the Einstein radius of a $10\,M_\odot$ microlens. This justifies the high sensitivity to objects with $0.1-0.3\,M_\odot$ and the need for longer trajectories to constrain the population of massive PBHs. The ODLCs also span ~20 Einstein radii of a Jupiter-mass microlens, making them extraordinarily sensitive to these planetary-mass objects for the most compact source.

As a general conclusion, variability and single-epoch studies of lensed quasars have great potential to constrain PBH populations, but the data, methodology, and targets used may play an important role. Future work with optical light curves[2] should be based on records with low observational noise and spanning tens of years (covering long trajectories in magnification maps), as well as reverberation-based source sizes and microlensing simulations with a fine resolution of the parameter grid (it might be required to use a double source; e.g. the accretion disc plus broad line region). There is also the pending task of probing the possible presence of PBHs along the line of sight to a given lensed quasar (e.g. Hawkins 2020, 2022, 2024) from complex simulations involving PBH populations at different redshifts.

Data availability

The light curves and Python scripts to create/show ODLCs are publicly available at `https://github.com/glendama/q0951odlc`, and the Fortran-90 code to generate magnification maps is publicly available at `https://github.com/glendama/magmaps`

Acknowledgements. We thank the anonymous referee for comments and suggestions which helped us to improve the manuscript. The Liverpool Telescope is operated on the island of La Palma by Liverpool John Moores University in the Spanish Observatorio del Roque de los Muchachos of the Instituto de Astrofísica de Canarias with financial support from the UK Science and Technology Facilities Council. AEG acknowledges support from project ANID Fondecyt Postdoctorado with grant number 3230554. JMD acknowledges support from project PID2022-138896NB-C51 (MCIU/AEI/MINECO/FEDER, UE) Ministerio de Ciencia, Investigación y Universidades. This research has been supported by Universidad de Cantabria funds and the grant PID2020-118990GB-I00 funded by MCIN/AEI/10.13039/501100011033.

References

Abbott, B. P., Abbott, R., Abbott, T. D., et al. 2019, Phys. Rev. X, 9, 031040
Awad, P., Chan, J. H. H., Millon, M., Courbin, F., & Paic, E. 2023, A&A, 673, A88
Bertone, G. 2010, Nature, 468, 389
Bhatiani, S., Dai, X., & Guerras, E. 2019, ApJ, 885, 77
Carr, B., & Kühnel, F. 2022, SciPost Phys. Lect. Notes, 48
Cornachione, M. A., Morgan, C. W., Burger, H. R., et al. 2020, ApJ, 905, 7
Dai, X., & Guerras, E. 2018, ApJ, 853, L27
Diego, J. M., Kaiser, N., Broadhurst, T., et al. 2018, ApJ, 857, 25
Eigenbrod, A., Courbin, F., & Meylan, G. 2007, A&A, 465, 51
Esteban-Gutiérrez, A., Agües-Paszkowsky, N., & Mediavilla, E. 2022, ApJ, 929, 123
Esteban-Gutiérrez, A., Mediavilla, E., & Jiménez-Vicente, J. 2023, ApJ, 954, 172
Eulaers, E., & Magain, P. 2011, A&A, 536, A44
Fian, C., Chelouche, D., & Kaspi, S. 2023, A&A, 677, A94
Gil-Merino, R., Goicoechea, L. J., Shalyapin, V. N., & Braga, V. F. 2012, ApJ, 744, 47
Gil-Merino, R., Goicoechea, L. J., Shalyapin, V. N., & Oscoz, A. 2018, A&A, 616, A118
Goicoechea, L. J., Shalyapin, V. N., & Oscoz, A. 2024, MNRAS, 530, 2273
Grogin, N. A., & Narayan, R. 1996, ApJ, 464, 92
Hawkins, M. R. S. 2020, A&A, 633, A107
Hawkins, M. R. S. 2022, MNRAS, 512, 5706
Hawkins, M. R. S. 2024, MNRAS, 527, 2393
Jakobsson, P., Hjorth, J., Burud, I., et al. 2005, A&A, 431, 103
Kelly, P. L., Diego, J. M., Rodney, S., et al. 2018, Nat. Astron., 2, 334
Kochanek, C. S. 2004, ApJ, 605, 58
Kochanek, C. S., Falco, E. E., Impey, C. D., et al. 2000, ApJ, 543, 131
Kochanek, C. S., Dai, X., Morgan, C., et al. 2007, ASP Conf. Ser., 371, 43
Mediavilla, E., Muñoz, J. A., Falco, E., et al. 2009, ApJ, 706, 1451
Mediavilla, E., Jiménez-Vicente, J., Muñoz, J. A., et al. 2017, ApJ, 836, L18
Mosquera, A. M., & Kochanek, C. S. 2011, ApJ, 738, 96
Mróz, P., Udalski, A., Szymański, M. K., et al. 2024, Nature, 632, 749
Mudd, D., Martini, P., Zu, Y., et al. 2018, ApJ, 862, 123
Paic, E., Vernardos, G., Sluse, D., et al. 2022, A&A, 659, A21
Paraficz, D., Hjorth, J., Burud, I., Jakobsson, P., & Elíasdóttir, Á. 2006, A&A, 455, L1
Peng, C. Y., Impey, C. D., Rix, H.-W., et al. 2006, ApJ, 649, 616
Rathna Kumar, S., Stalin, C. S., & Prabhu, T. P. 2015, A&A, 580, A38
Rivera, A. B., Morgan, C. W., Florence, S. M., et al. 2023, ApJ, 952, 54
Rubin, V. C., Ford, W. K., & Thonnard, N. 1978, ApJ, 225, L107
Rubin, V. C., Ford, W. K., & Thonnard, N. 1980, ApJ, 238, 471
Ruiz-Hinojosa, E. 2023, Master Thesis, Univ. Cantabria
Schechter, P. L., Gregg, M. D., Becker, R. H., Helfand, D. J., & White, R. L. 1998, AJ, 115, 1371
Schneider, P., Ehlers, J., & Falco, E. E. 1992, Gravitational Lensing (Berlin: Springer)
Shalyapin, V. N., Goicoechea, L. J., Koptelova, E., et al. 2009, MNRAS, 397, 1982
Shalyapin, V. N., Gil-Merino, R., & Goicoechea, L. J. 2021, A&A, 653, A121
Shalyapin, V. N., Goicoechea, L. J., & Ruiz-Hinojosa, E. 2025, A&A, 694, A31
Sluse, D., Chantry, V., Magain, P., Courbin, F., & Meylan, G. 2012, A&A, 538, A99
Tuntsov, A. V., Lewis, G. F., & Walker, M. A. 2024, MNRAS, 528, 1979
Vernardos, G., Sluse, D., Pooley, D., et al. 2024, Space Sci. Rev., 220, 14
Wilson, M. L., Zabludoff, A. I., Keeton, C. R., et al. 2017, ApJ, 850, 94

[2] It would also be desirable to have X-ray flux time series to constrain populations of sub-Jupiter mass PBHs.

Appendix A: Summary of the physical scenarios

Table A.1. 30 compositions of the lensing galaxy for each of the three source sizes: $r_s = 0.605$ (largest), 0.276 (intermediate), and 0.1 (smallest).

f_{sdmG}	F_{pbhG}	f_{starG}	f_{pbhG}	r_{pbh}
0.1	0.0	0.90	0.00	—
	0.1	0.81	0.09	−2.5
				−0.5
				+1.5
	0.5	0.45	0.45	−2.5
				−0.5
				+1.5
	0.9	0.09	0.81	−2.5
				−0.5
				+1.5
0.5	0.0	0.50	0.00	—
	0.1	0.45	0.05	−2.5
				−0.5
				+1.5
	0.5	0.25	0.25	−2.5
				−0.5
				+1.5
	0.9	0.05	0.45	−2.5
				−0.5
				+1.5
0.9	0.0	0.10	0.00	—
	0.1	0.09	0.01	−2.5
				−0.5
				+1.5
	0.5	0.05	0.05	−2.5
				−0.5
				+1.5
	0.9	0.01	0.09	−2.5
				−0.5
				+1.5

Note: f_{sdmG}, f_{starG}, and f_{pbhG} are the mass fractions of the galaxy G in SDM, stars, and PBHs, respectively. The stellar mass function follows a Kroupa distribution with a mean mass $M_{star} = 0.3\,M_\odot$, while all PBHs have the same mass M_{pbh}, where $r_{pbh} = \log(M_{pbh}/M_{star})$. The relative radius r_s is the ratio between the source radius and the Einstein radius (in the source plane) of a typical star with the mean mass M_{star}.

Appendix B: Comparing the consistency probability with a simple Bayesian metric

In this study we used a dataset ODLC to draw inferences about a physical scenario s. Thus, in a Bayesian framework for quasar microlensing (e.g. Kochanek et al. 2007), the probability of a pair of trajectories τ in the two magnification maps for s given the data is

$$P(s,\tau|\mathrm{ODLC}) \propto P(\mathrm{ODLC}|s,\tau) \propto \exp[-\chi^2(s,\tau)/2], \quad \text{(B.1)}$$

where $P(\mathrm{ODLC}|s,\tau)$ is the likelihood of the data given (s,τ) and

$$\chi^2(s,\tau) = \sum_{j=1}^{N} \left[\frac{O_j - S_j(s,\tau)}{E_j}\right]^2. \quad \text{(B.2)}$$

We computed the χ^2 value of each SDLC for s, and then estimated the probability of the scenario s by marginalising over all trajectories. This means we summed the probabilities for the randomly sampled trajectories to obtain

$$P(s|\mathrm{ODLC}) \propto \sum_{\tau} \exp[-\chi^2(s,\tau)/2]. \quad \text{(B.3)}$$

Using formal photometric errors E_j, as expected, the SDLCs failed to reproduce the overall variability of the ODLCs, since the χ^2/N values exceeded 2.5 (first approach) and 2.7 (second approach). When increasing errors by a factor $1.5\times RMS\,(\mathrm{L})$ (see the second analysis scheme in Sect. 3.3), we calculated probabilities relative to a reference scenario s_*: $\eta(s) = P(s|\mathrm{ODLC})/P(s_*|\mathrm{ODLC})$, where s_* is the standard scenario consisting of a lensing galaxy with 10% of mass in stars and the intermediate size source (see the top panels of Figures 2 and 3). The $\eta(s)$ values were then compared with the relative probabilities from the CP metric, i.e., $\epsilon(s) = CP(T)/CP_*(T)$, where CP_* is the consistency probability for s_* and $T = 1.5\times RMS\,(\mathrm{L})$. Figure B.1 shows our results for both approaches using the two metrics. These results are discussed at the end of Sect. 4.

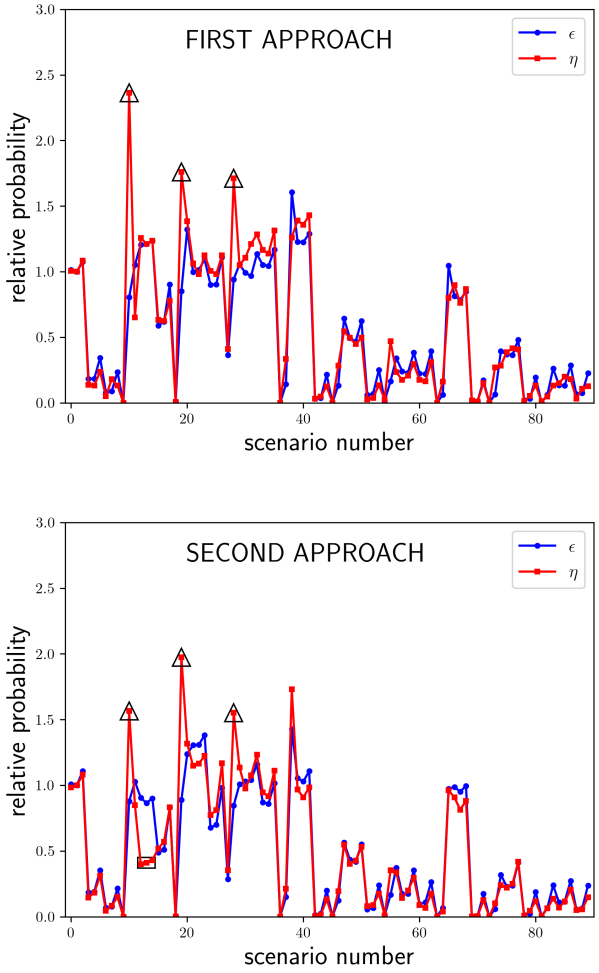

Fig. B.1. Relative probabilities from two different metrics. Considering the two approaches in Table 1, we compare the values of ϵ and η for each of the 90 physical scenarios summarised in Appendix A. The values of η for the same three scenarios in both approaches are highlighted with black triangles. We also use a black rectangle to highlight the values of η for three other scenarios in the second approach (see the main text).